
Loss shaping enhances exact gradient learning with Eventprop in Spiking Neural Networks

Thomas Nowotny*

School of Engineering and Informatics
University of Sussex
Brighton, BN1 9QJ, UK
T.Nowotny@sussex.ac.uk

James P. Turner

Information & Communication Technologies
Imperial College London
London, SW7 2AZ, UK
james.turner@imperial.ac.uk

James C. Knight

School of Engineering and Informatics
University of Sussex
Brighton, BN1 9QJ, UK
J.C.Knight@sussex.ac.uk

Abstract

Event-based machine learning promises more energy-efficient AI on future neuromorphic hardware. Here, we investigate how the recently discovered Eventprop algorithm for gradient descent on exact gradients in spiking neural networks can be scaled up to challenging keyword recognition benchmarks. We implemented Eventprop in the GPU-enhanced Neural Networks framework and used it for training recurrent spiking neural networks on the Spiking Heidelberg Digits and Spiking Speech Commands datasets. We found that learning depended strongly on the loss function and extended Eventprop to a wider class of loss functions to enable effective training. When combined with the right additional mechanisms from the machine learning toolbox, Eventprop networks achieved state-of-the-art performance on Spiking Heidelberg Digits and good accuracy on Spiking Speech Commands. This work is a significant step towards a low-power neuromorphic alternative to current machine learning paradigms.

1 Introduction

Modern deep neural networks need kilowatts of power to perform tasks that the human brain can do on a 20W power budget. One of the ways the brain achieves this efficiency is through event-based “spiking” information processing, which has inspired research into neuromorphic computing. For instance, using this paradigm, the DYNAPs chip can simulate networks of 1024 neurons with a power budget of a milliwatt [30]. However, for a long time there had been doubts whether spiking neural networks (SNNs) can be trained by gradient descent, the gold standard in machine learning, due to the non-differentiable jumps of the membrane potential when spikes occur. Using approximations and simplifying assumptions and building up from single spikes and layers, gradient-based learning in SNNs has gradually been developed over the last 20 years, including the early SpikeProp algorithm [3] and its variants [27, 4, 47, 48, 31], also applied to deeper networks [25, 45, 39], the Chronotron [12], the (multispike) tempotron [16, 36, 15, 11], the Widrow-Hoff rule-based ReSuMe algorithm [35, 41, 56] and PSD [53], as well as the SPAN algorithm [28, 29] and Slayer [40]. Other approaches have tried to relate back-propagation to phenomenological learning rules such as STDP [43], to enable

*Corresponding Author

Free dynamics	Transition condition	Jumps at transition
Forward:		
(i) $\tau_{\text{mem}} \dot{V} = -V + I$	$(V)_n - \vartheta = 0,$	$(V^+)_n = 0$
(ii) $\tau_{\text{syn}} \dot{I} = -I$	$(\dot{V})_n \neq 0$	$I^+ = I^- + W e_n$
Backward:		
(iii) $\tau_{\text{mem}} \lambda'_V = -\lambda_V - \frac{\partial l_V}{\partial V}$	$t - t_k = 0$	(v) $(\lambda_V^-)_{n(k)} = (\lambda_V^+)_{n(k)} + \frac{1}{\tau_{\text{mem}} (\dot{V}^-)_{n(k)}} \left[\vartheta (\lambda_V^+)_{n(k)} \right.$
(iv) $\tau_{\text{syn}} \lambda'_I = -\lambda_I + \lambda_V$		$\left. + (W^T (\lambda_V^+ - \lambda_I))_{n(k)} + \frac{\partial l_p}{\partial t_k} + l_V^- - l_V^+ \right]$
Gradient of the loss: (vi) $\frac{d\mathcal{L}}{dw_{ji}} = -\tau_{\text{syn}} \sum_{t \in t_{\text{spike}}(i)} \lambda_{I,j}(t)$		

Table 1: Original Eventprop gradient calculation, adapted from Wunderlich and Pehle [46]. V and I are the membrane potential and input current and λ_V and λ_I the corresponding adjoint variables. τ_{mem} and τ_{syn} are the membrane and synaptic time constants. W is the weight matrix and ϑ the firing threshold. The dot denotes the derivative with respect to time and the prime the derivative backwards in time. Superscript “-” and “+” denote the values before and after a discontinuous jump. l_p and l_V are defined by the loss function, Wunderlich and Pehle [46], equation (1).

gradient descent by removing the abstraction of instantaneous spikes [18], or using probabilistic interpretations to obtain smooth gradients [10]. More recently, new algorithms in two main categories have been discovered. Many groups are proposing gradient descent-based learning rules that employ a surrogate gradient [54, 19, 1] while others have developed novel ways of calculating exact gradients [46, 13, 14, 5]. The arrival of these new methods has made gradient-based learning a realistic prospect and could enable a transition to low-energy neuromorphic machine learning. However, nobody has yet demonstrated which methods can be scaled to real-world problems. In this paper we investigate scaling up Eventprop learning [46] to larger benchmark problems. Eventprop leverages the adjoint method from optimisation theory, to calculate exact gradients in a backward pass that is – like the forward pass – a hybrid system of *per neuron* dynamical equations and discrete communication between neurons that only occurs at the times of sparse recorded spikes (table 1). Besides using exact gradients rather than approximations, which some may find attractive, Eventprop has therefore also attractive properties in terms of numerical efficiency, in particular for parallel computing: existing parallel algorithms for SNN simulation – whose compute complexity scales predominantly with the number of neurons rather than the number of synapses – can be employed for both forward and backward passes, and memory requirements only grow with the number of spikes rather than the number of timesteps in the trial, in contrast to commonly used versions of error back-propagation through time (BPTT).

We have implemented Eventprop in the GPU enhanced neural networks framework (GeNN) [50, 21] using the Python interface PyGeNN [23] and, here, performed simulations using the CUDA backend for NVIDIA GPUs. Our code is available on Github [33].

We first reproduced the latency encoded MNIST [24] classification task before moving on to the more challenging Spiking Heidelberg Digits (SHD) and Spiking Speech Commands (SSC) keyword recognition datasets [6]. When working on the SHD dataset we noticed issues that arise from using the exact gradient for particular combinations of loss functions and task attributes. To overcome this, we extended Eventprop to a wider class of loss functions and, using this additional freedom, identified better-performing formulations of cross-entropy loss, including one that leads, in conjunction with augmentation, to state-of-the-art performance on SHD. We then successfully applied the same network to SSC.

2 Results

We first reproduced the results of Wunderlich and Pehle [46] on the latency-encoded MNIST dataset [24] (S1) using the average cross-entropy loss

$$\mathcal{L}_{x\text{-entropy}} = -\frac{1}{N_{\text{batch}}} \sum_{m=1}^{N_{\text{batch}}} \int_0^T \log \left(\frac{\exp(V_{l(m)}^m(t))}{\sum_{k=1}^{N_{\text{class}}} \exp(V_k^m(t))} \right) dt, \quad (1)$$

where N_{batch} is mini-batch size, m the trial index, T the trial duration, V_*^m the output voltage of output $*$ in the m th trial, and $l(m)$ the correct class label. We used a three-layer feedforward LIF network (784 – 128 – 10 neurons) and achieved a similar classification performance on the test set ($97.8 \pm 0.1\%$ correct – mean \pm standard deviation in $n = 10$ repeated runs) as Wunderlich and Pehle [46] ($97.6 \pm 0.1\%$ correct). This independently reproduces their work and demonstrates that our discrete-time implementation with 1 ms timesteps is precise enough to achieve the same performance as their event-based simulations in this task.

We then considered SHD. We again used $\mathcal{L}_{x\text{-entropy}}$ to train a variety of three-layer networks with differently sized hidden layers with and without recurrent connectivity, and with a variety of meta-parameter values. However, the trained networks only performed close to chance level (e.g. training performance $10.9 \pm 1.3\%$ correct ($n = 10$) after 200 epochs for a feedforward network with 256 hidden neurons. Chance level is 5%). To understand this failure, we inspected the learning dynamics of the network in more detail. Through inspection of table 1 equations (v),(iii),(iv) and (vi) it is clear that hidden neurons that have a positive weight towards the corrected output neuron will receive less excitation after learning updates when $\lambda_V - \lambda_I$ is less than 0 in a trial, and those with negative weight will receive more. Figure 1A-E shows an example of a typical trial in the early learning phase. In this example, an input of class 0 was shown but output 0 was not the highest. Hence, $\lambda_{V,0}$, and hence $\lambda_{I,0}$ increase in the backward pass during the period where input and hidden spikes had occurred. This leads to transported error signals $\lambda_{V,0} - \lambda_{I,0}$ that are on average less than 0 (Figure 1D, E and therefore decreased the drive of hidden neurons with a positive weight to the correct output 0 and increased drive of neurons with negative weights to output 0. In other words, the neurons that are driving the correct output are gradually switched off and those that suppress the correct output are switched on – opposite to what one would expect. Close inspection of Figure 1E illustrates that the negative error signal stems from the sharp drop of λ_V in backwards time, related to the sudden onset of spikes at the beginning of the trial and the preceding silent period. Similar effects occur for correct trials and the trailing silent period as well.

To investigate this effect more explicitly we trained the network with input class 0 only and inspected the activity of hidden neurons and their weights towards the correct output 0. The number of spikes in the hidden neurons after training (Figure 1G and their output weights onto output 0 (Figure 1F) are strongly negatively correlated, Pearson correlation coefficient -0.707 . The highest output weights are from hidden neurons that no longer respond to the class of inputs that the output neuron is supposed to represent – they have been switched off due to the gradient descent in the hidden layer.

Fundamentally, the learning failure is caused by the absence of information about the creation or deletion of spikes in the exact gradient and the structure of the loss function that aims to minimise cross-entropy at *all* times during the trial, even during the silent periods at the start and end. Accordingly, if we remove the silent period by training the network on the first 400 ms of each SHD digit, we see a somewhat better training performance ($30.2 \pm 1.2\%$ correct ($n = 10$)).

To avoid the problems incurred with $\mathcal{L}_{x\text{-entropy}}$ altogether we need to remove the arguably unnecessary goal of being able to make a correct classification at all times during the trial, particularly where this is impossible due to periods of silence. A natural loss function to consider with this goal in mind is the cross-entropy of the sum or integral of the membrane potentials of non-spiking output neurons, which has been used widely with BPTT [55],

$$\mathcal{L}_{\text{sum}} = -\frac{1}{N_{\text{batch}}} \sum_{m=1}^{N_{\text{batch}}} \log \left(\frac{\exp \left(\int_0^T V_{l(m)}^m(t) dt \right)}{\sum_{k=1}^{N_{\text{out}}} \exp \left(\int_0^T V_k^m(t) dt \right)} \right), \quad (2)$$

where V_k^m is the membrane potential of output k in trial m and T trial duration. With \mathcal{L}_{sum} , the contribution of each spike has (almost) no dependency on when it occurs so that there is (almost) no

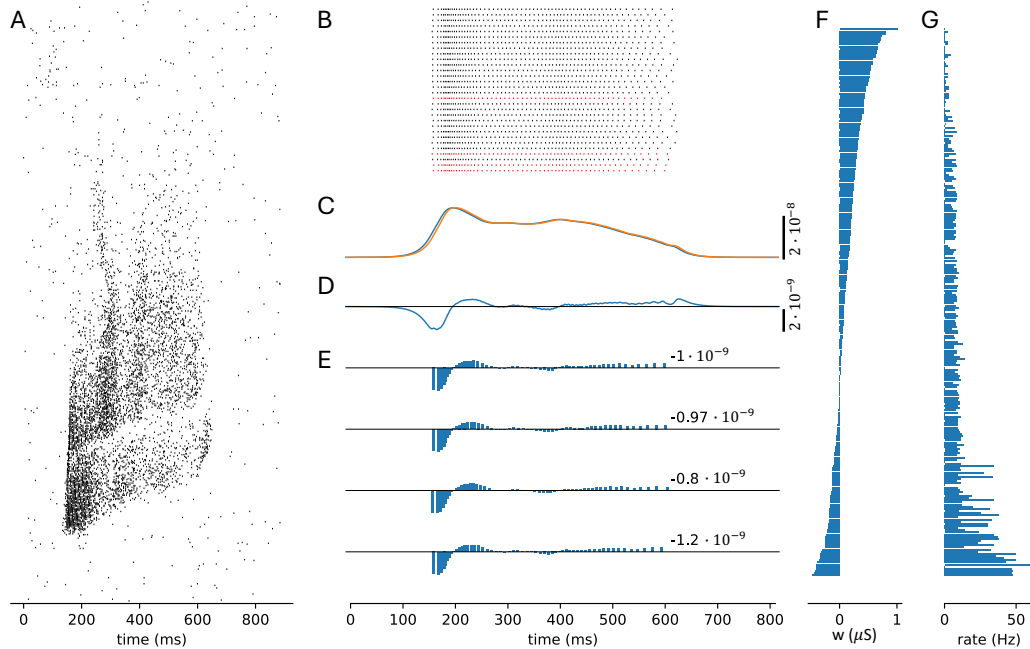


Figure 1: Illustration of the mechanism that leads to unhelpful spike deletions in hidden neurons. **(A)** Spike raster of a typical input pattern of class 0. **(B)** Spike raster of the hidden layer in response to an input of class 0 (showing a subset of 30 of 256 neurons for better visibility). Red highlighted neurons are those that are most active on average for class 0 inputs and correspond to the panels shown in E. **(C)** λ_V (orange), λ_I (blue) of output neuron 0 in the corresponding backwards pass plotted against forward time, i.e. integration proceeds from the right to the left. During backwards integration, λ_V increases rapidly from 0 to the value corresponding to all output voltages being 0 and λ_I follows λ_V (around $t=1400$, not shown). When the stored spikes are encountered, λ_V , λ_I increase further as the model is not yet trained and the correct output voltage does not dominate in the response. **(D)** The difference $\lambda_V - \lambda_I$ of output 0 that is transported to the neurons in the hidden layer. **(E)** $\lambda_V - \lambda_I$ values arriving at the four most active neurons (marked in red in B) when transported during a stored spike, shown as bars. The numbers indicate the sum of all bars, which relates to the direction of the total change in excitation the hidden neurons receive. All values are negative, i.e. neurons with positive weights towards the correct output 0 will become less activated for this and similar inputs of class 0 after the learning update and hidden neurons with negative weight will become more active – exactly opposite to what one would expect for efficient learning. **(F)** distributions of weights from hidden neurons onto neuron 0 after 30 epochs of training on class 0. **(G)** Average firing rate of hidden neurons, in response to inputs of class 0 during the last mini-batch of the same training. Neurons are in the same order in F and G (sorted by their weight onto output 0).

pressure for changes to hidden neurons, avoiding the learning failure. However, \mathcal{L}_{sum} is not supported in the normal Eventprop framework prompting us to extend it.

2.1 Additional loss functions in Eventprop

We extend Eventprop to losses of the shape

$$\mathcal{L}_F = F \left(\int_0^T l_V(V(t), t) dt \right), \quad (3)$$

where F is differentiable and l_V can be vector-valued, e.g. $l_V = V$ as in the loss functions used below. Using the chain rule and re-organising terms in an appropriate way we can derive an extended scheme that is identical to the original Eventprop method except that equation (iii) in table 1 is replaced by

$$\tau_{\text{mem}} \lambda'_{V,j} = -\lambda_{V,j} - \frac{\partial F}{\partial (\int l_V dt)} \cdot \frac{\partial l_V}{\partial V_j}. \quad (4)$$

See Appendix A for a detailed derivation. Equipped with the extended scheme, we implemented loss functions for classifying based on the sum of integrated membrane voltage of non-spiking output neurons (2) or on the maximum, as in Wunderlich and Pehle [46], equation (4). We also compare against using spiking output neurons and classifying depending on the first spike with the loss from Wunderlich and Pehle [46], equation 3. We found that all loss functions performed reasonably well for the latency MNIST task, with a slightly lower performance when using $\mathcal{L}_{\text{time}}$ (Figure S1).

2.2 Spiking Heidelberg Digits

We then returned to the SHD benchmark. We optimised the meta-parameters of the models with each of the loss functions using grid searches in a 10-fold cross-validation approach: In each fold, we trained the network on 9 of the speakers and tested it on the examples spoken by the 10th speaker (see tables 3, 4). Then, we measured training and testing performance with the full training- and test set. The results are shown in Figure 2.

Apart from the completely failing $\mathcal{L}_{x\text{-entropy}}$ loss, the worst performance and least reliability was observed for $\mathcal{L}_{\text{time}}$, followed by \mathcal{L}_{max} . \mathcal{L}_{sum} performed competitively with respect to the results reported in the literature [55] and the e-prop results obtained in our lab [22], especially when used with recurrent connectivity. However, the performance was not quite as good as the competitors and, when we inspected the learning dynamics, we observed that learning for \mathcal{L}_{sum} is comparatively slow despite an increased learning rate $\lambda = 2 \cdot 10^{-3}$ (see table 4). The optimised regularisation strength of the hidden layer is also orders of magnitudes smaller in this model than in others. Both observations indicate that the gradients flowing from the output towards the hidden layer are very small. On reflection, this effect can be easily understood when realising that, due to the definition of \mathcal{L}_{sum} , the timing of hidden spikes has (almost) no effect on their contribution to the overall loss. Every post-synaptic potential (PSP) causes the same added (or subtracted for negative synaptic weight) area under the membrane potential and hence the same increase or reduction in loss. The only PSPs for which this is not the case are those that are ‘cut off’ at trial end. By moving *these* PSPs forwards or backwards in time, the amount cut off their area can be changed, resulting in tiny contributions to the gradient.

Based on this insight, we improved the gradient flow to the hidden layer by adding a weighting term to \mathcal{L}_{sum} that would make earlier PSPs more effective for increasing or reducing loss. We tried four different weightings, linearly decreasing, exponentially decreasing, sigmoid and proportional to the number of input spikes at each timestep. From numerical experiments, we found the best-performing weighting to be the exponential weighting,

$$\mathcal{L}_{\text{sum_exp}} = -\frac{1}{N_{\text{batch}}} \sum_{m=1}^{N_{\text{batch}}} \log \left(\frac{\exp \left(\int_0^T e^{-t/T} V_{l(m)}^m(t) dt \right)}{\sum_{k=1}^{N_{\text{out}}} \exp \left(\int_0^T e^{-t/T} V_k^m(t) dt \right)} \right). \quad (5)$$

As shown in Figure 2 this leads to accuracies comparable with previous SNN results with BPTT [55] and our own results with e-prop [22].

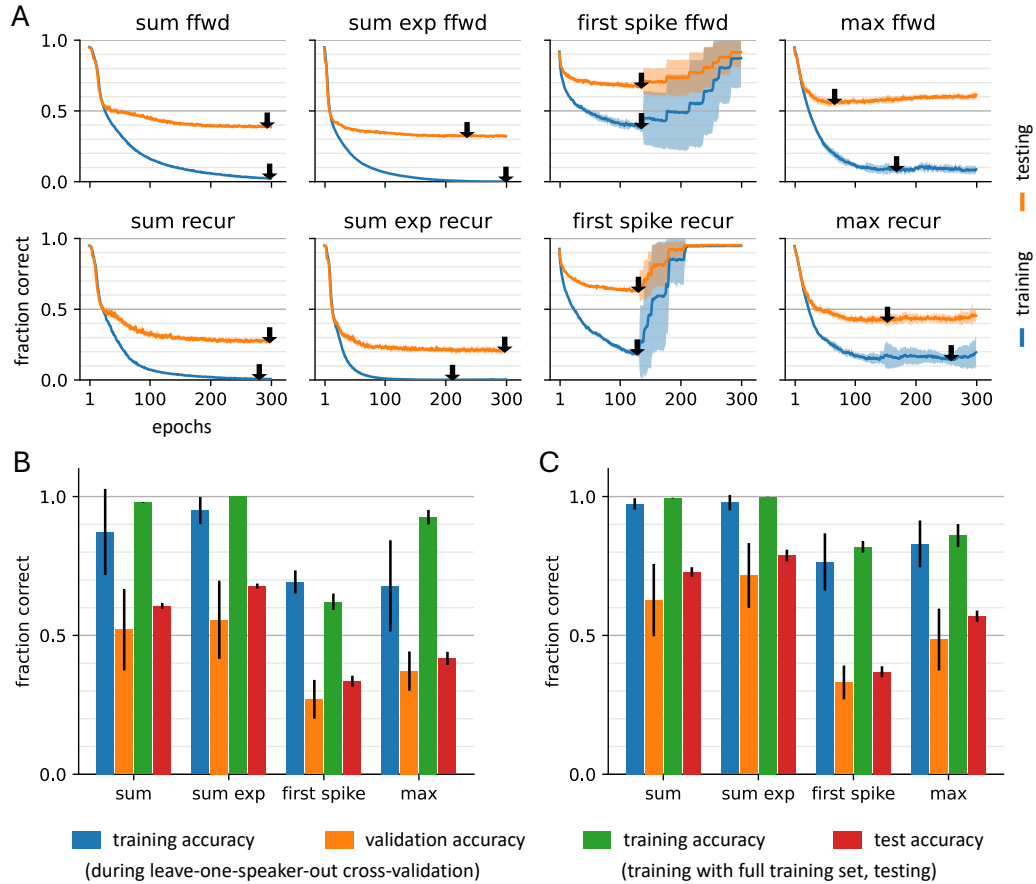


Figure 2: Summary of initial SHD classification results with a simple network, including regularisation only. **(A)** Learning curves for training (blue) and testing error (orange). "fwd" are feed-forward networks, "recur" recurrent networks. Curves are the mean of 8 repeated runs with different random seeds and shaded areas indicate one standard deviation around the mean. The arrows indicate the location of the best-achieved training or validation error. **(B)** average accuracies in feedforward networks at the epoch with the best validation error for cross-validation and at the epoch with the best training error for train/test. Values are the average across 10 folds in leave-one-speaker-out cross-validation and the average across 8 independent runs for train/test. Error bars are the corresponding standard deviations. **(C)** as B but for recurrent networks. The results for the failing $\mathcal{L}_{x\text{-entropy}}$ loss were omitted in this figure to avoid too much clutter.

2.3 Applying machine learning tools for better accuracy

Once we overcame the major obstacle of finding an appropriate loss function, we applied tools from the machine learning toolbox to maximise final test accuracy. First, we applied four different types of data augmentation (see methods for details): Global random shifts across input channels, randomly re-assigning individual spikes to nearby input channels, compressing or dilating the duration of stimuli and generating new input patterns by blending together two random examples of the same class. Only “shift” and “blend” augmentations proved effective.

Next, we investigated different network structures, including different hidden layer sizes, multiple hidden layers and a “delay line” where 10 copies are made of each input neuron and copy n is activated with a delay of $n \cdot 30$ ms. All networks had fully recurrent hidden layers based on the observations above. We found that multiple layers did not improve accuracy and did not pursue this further.

We also investigated the role of the simulation timestep, noting that competitors are using timesteps as large as 10 ms [17] or even 25 ms [2]. We found that 1ms and 2ms timesteps performed best, with acceptable results for 5 ms steps but clear degradation for 10 ms (see figure S2).

Finally, we derived equations for training timescales τ_{mem} and τ_{syn} (see appendix C) and investigated homogeneous and heterogeneous initialisation for timescale parameters following Perez-Nieves et al. [34].

As a result of our extensive experimentation, we achieved the maximum cross-validation accuracy of 92% and, for the same parameters, $93.5 \pm 0.7\%$ test accuracy ($n = 8$).

We then investigated the contributions of the different mechanisms to classification accuracy in an ablation experiment. We started from the best solution and scanned the following parameters in all combinations: blend augmentation, shift augmentation, delay line, initialisation of τ and training τ , using a rigorous validation methodology (see methods). Figure 3A shows the results. Without data augmentations or input delay line (Fig 3A “plain”, blue), we barely surpass 80% accuracy and the size of the hidden layer is important for better performance. Adding heterogeneous τ values and doing so in conjunction with τ learning improves the results in agreement with earlier results [34]. Adding the augmentations, the networks fall into two clusters of medium performance networks (“blend”, “shift”, “shift+blend”, “delay”) and best performance networks (“delay+blend”, “delay+shift”, “delay+shift+blend”). In this group of best performers, the hidden layer size matters less – even a network with only 64 hidden units can achieve almost 90% test accuracy – and, interestingly, the advantages of heterogeneous τ and τ learning completely disappear. As Perez-Nieves et al. [34] were operating in the lower accuracy regime of our “plain” network, this is consistent with their results but casts a different light on the overall assessment of the importance of heterogeneity and timescale learning.

We then analysed the time taken to train the different networks in comparison to test accuracy (Figure 3B). Unsurprisingly, there is a clear positive correlation between high accuracy and high runtime. Interestingly, however, there are networks with considerably lower than maximum runtime and yet almost the best accuracy (512 hidden neurons, “delay+shift” and “delay+shift+blend” – fat crosses and pluses in red).

When comparing test accuracy to the number of trained parameters (Figure 3C), clearly more parameters typically lead to better results, though this levels out for networks larger than 512 hidden neurons. Even some of the networks with 128 hidden neurons and less than 1 million parameters are still competitive.

2.4 Spiking Speech Commands

To test the generality of our observations, we also classified the words in the spiking speech commands (SSC) dataset [6]. The SSC dataset consists of the Google speech commands data [44], encoded using the same cochlea model used for SHD.

In preliminary experiments using “plain” networks, we observed that, unlike SHD, the SSC dataset is prone to underfitting. This indicated that these networks were too small to fully capture this data. However, after adding the additional delay-line input described above, more typical over-fitting was observed that we again addressed with augmentations.

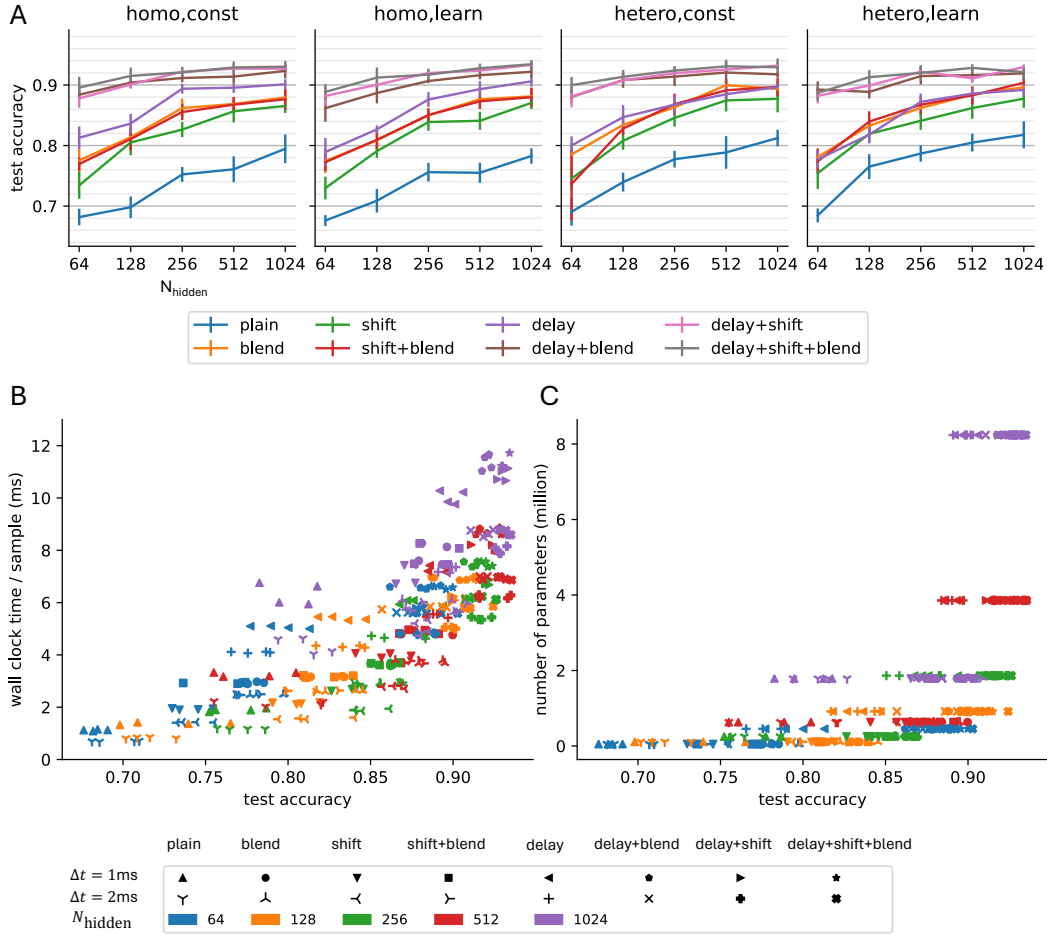


Figure 3: Ablation study on the SHD dataset. **(A)** accuracy on the test set as mean (line) and standard deviation (errorbars) of 8 independent runs with different random number seeds. The panels are for different combinations of homogeneous and heterogeneous initialisation of τ_{mem} and τ_{syn} and for static or trained τ values as indicated. The different coloured lines correspond to the different augmentations applied as shown. **(B)** Wall clock time per sample during training as a function of test accuracy for all the different conditions as indicated by the symbols and colours. This data includes runs with $\Delta t = 1\text{ms}$ and $\Delta t = 2\text{ms}$. **(C)** Number of parameters, including tau values where trained, of the different networks as a function of the final test accuracy. Both B and C use the mean accuracy over 8 independent runs as in A.

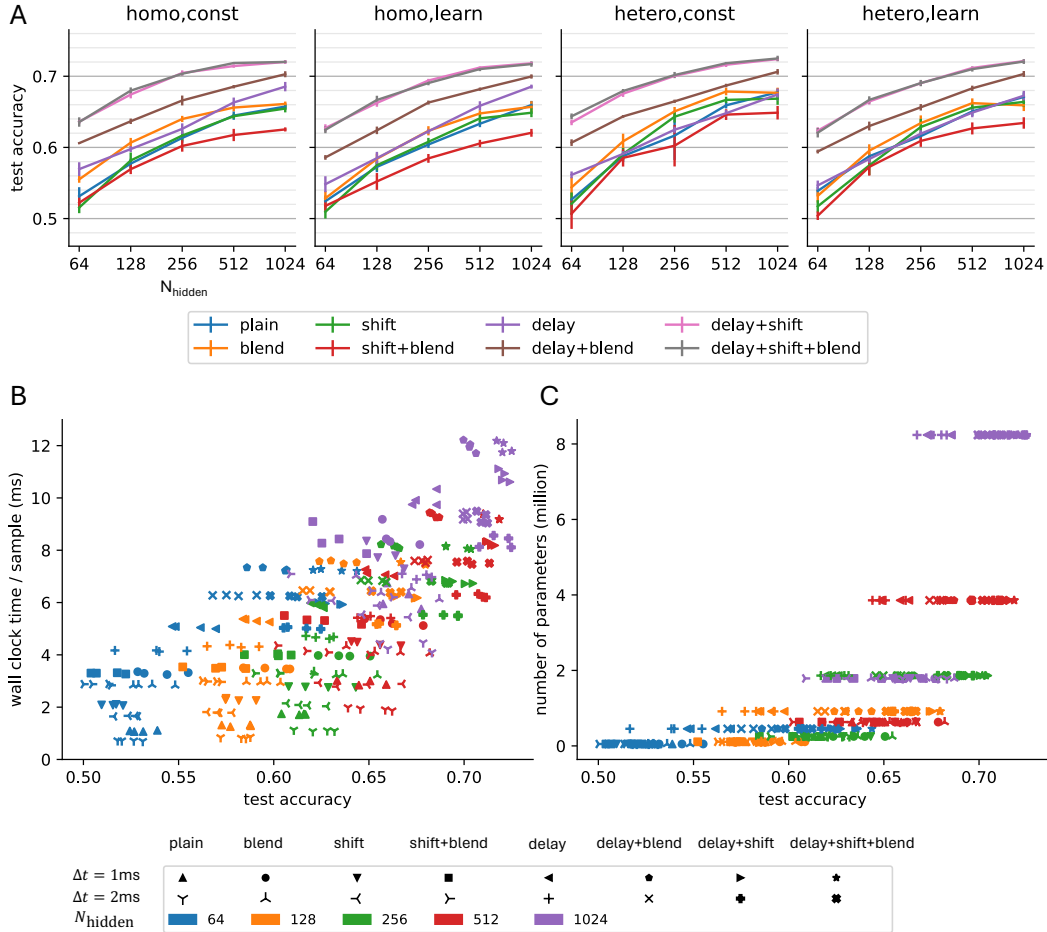


Figure 4: Ablation study on the SSC dataset. A) accuracy of classification, B) wall clock time versus accuracy, C) number of parameters versus accuracy, all as in figure 3

For SSC we obtained the best validation performance (early stopping) of 74.7% and for the parameter set in question $74.1 \pm 0.9\%$ test accuracy as measured in 8 independent runs.

We then again performed a rigorous ablation study (figure 4A to analyse the contributions of the different augmentations). Here, heterogeneous and learnt τ_{mem} and τ_{syn} do not appear to have much effect. The networks get better with more augmentations, except for the “blend” augmentation which does not seem to be very effective on SSC and even reduces test accuracy when used on its own (red lines versus blue lines in figure 4A. This may be because SSC is obtained from a much larger number of speakers so adding additional examples obtained by “blend” is both less important and – if blended examples are made from very different examples – could produce unhelpful out-of-distribution examples. Another difference to the observations on SHD is that the hidden layer size remains important, even for the best-performing networks, likely reflecting that SSC is a harder dataset. We also note that there is an even stronger separation than for SHD with “delay+shift” and “delay+shift+blend” clearly achieving significantly higher accuracy than any of the other networks.

When analysing runtime as a function of test accuracy (figure 4B), we see the same trends as for SHD, though the cloud of data points is broader, reflecting the more pronounced differences in test accuracy between networks. Also, for SSC, the largest networks (purple) are more clearly achieving the best accuracy but there are networks that work equally well with $\Delta t = 2\text{ms}$ (purple fat pluses) as with $\Delta t = 1\text{ms}$ which offers some reduction in computational costs. When comparing the number of parameters and test accuracy (figure 4C), the relationship is clear with larger numbers of parameters leading to higher accuracy although it is worth noting that, between models with the same number of parameters, there are marked differences in the accuracy they achieve.

3 Discussion and Conclusions

In this article, we have presented learning results for the Eventprop algorithm implemented in GeNN. We have identified issues when training spiking neural networks using the exact gradient calculated with Eventprop and the average cross-entropy loss function $\mathcal{L}_{x\text{-entropy}}$ on the SHD dataset. As explained in detail in the Results, this loss function led to the silencing of the most relevant hidden neurons. We overcame the problems by deriving an extended Eventprop algorithm that allows more general loss functions and found that the cross-entropy loss of average output voltages \mathcal{L}_{sum} allowed successful learning but learning was slow and somewhat unreliable. We identified that this was due to an almost complete lack of gradient flow towards the hidden layer, so went full circle and augmented \mathcal{L}_{sum} with a beneficial weighting term (resulting in $\mathcal{L}_{\text{sum_exp}}$) and *finally* observed fast and reliable learning on the SHD dataset.

In parallel, several competing works on training SNNs for SHD and SSC datasets have been published, which use additional mechanisms and tools and achieve accuracy of up to 95.1% on the SHD test set [9, 49, 52, 42, 2, 17, 38]. We, therefore, investigated several augmentations of our RSNN networks and achieved the $93.5 \pm 0.7\%$ test accuracy reported above. This is less than some of the works listed, but some studies [38, 2, 17] used the test set as a validation set, including for early stopping and the methodology employed in others [42, 52, 52, 49] is unclear whereas we here followed a strict procedure of finding parameters through 10-fold leave-one-speaker-out cross-validation and then training on the entire training set with early stopping on the training accuracy. Only then did we evaluate the performance on the test set. With a looser approach, we could have reported the highest observed test accuracy during our ablation study which was 95.5% – on par with the best competitors – but that would constitute overfitting of the test set [32]. Interestingly, our results are very similar to D’Agostino et al. [9] who also used a proper validation strategy (random 80%/20% training/validation split on the original training set).

On the SSC dataset, we achieved an accuracy of $74.1 \pm 0.9\%$ whereas competitors using SNNs augmented with various additional mechanisms have achieved test accuracies of up to 80.29% [37, 51, 7, 2, 17]. Finally, although it is not technically an SNN, Schöne et al. [38] achieved 87.1% with an event-driven deep state space model. It is possible that, for the SSC dataset, the additional mechanisms proposed by the competitors make a measurable difference but we speculate that surrogate gradient descent with BPPT on large timesteps (up to 25 ms) is reducing the long-time dependencies in the data and thus simplifying the temporal credit-assignment problem. It is debatable, however, whether this still constitutes an SNN and how it would fare on neuromorphic hardware as, inevitably, a very large proportion of neurons will spike during each large timestep. It will also be interesting to see how different approaches compare on future datasets that may depend more strongly on exact spike timings so that the distinct advantage of Eventprop to allow a very large number of timesteps (and hence temporal precision), especially in the efficient GeNN implementation, may come to full fruition.

The Eventprop implementation in GeNN introduced in this paper is efficient and utilizes GeNN’s advanced algorithms for event propagation in both the forward and backward passes. Nevertheless, a full 10-fold cross-validation with 100 epochs per fold still takes several hours on an A100 GPU highlighting that this type of research remains compute-intensive. A detailed comparison of runtimes with those of other learning rules will be published separately.

In conclusion, while the ability to calculate exact gradients efficiently using the EventProp method is attractive, the exact gradient is agnostic to spike creation and deletion and this can lead to learning failures in some combinations of task and loss function. In this paper, we have overcome these problems by extending EventProp to more general loss functions. We have demonstrated on the SHD benchmark how ‘loss shaping’, i.e. choosing a bespoke loss function that induces beneficial gradient flows and learning dynamics, allows us to scale up Eventprop learning beyond proof of concept examples. Whether loss shaping can be done in a more principled way and how it carries over to deeper networks are open questions we would like to address in the near future. We are also planning to combine Eventprop with advanced network architectures beyond fully recurrent hidden layers which are known to struggle with learning long-time dependencies.

Acknowledgments and Disclosure of Funding

We thank Christian Pehle for his feedback on Appendix C and Christopher L Buckley for helpful comments on the manuscript. This work was funded by the EPSRC (Brains on Board project, Grant Number EP/P006094/1, ActiveAI project, Grant Number EP/S030964/1, Unlocking spiking neural networks for machine learning research, Grant Number EP/V052241/1) and the European Union’s Horizon 2020 research and innovation programme under Grant Agreement 945539 (HBP SGA3). Additionally, we gratefully acknowledge the Gauss Centre for Supercomputing e.V. (www.gauss-centre.eu) for funding this project by providing computing time through the John von Neumann Institute for Computing (NIC) on the GCS Supercomputer JUWELS at Jülich Supercomputing Centre (JSC); and the JADE2 consortium funded by the EPSRC (EP/T022205/1) for compute time on their systems.

4 Methods

4.1 Phantom spike regularisation

For the time to first spike loss function $\mathcal{L}_{\text{time}}$, there is a risk that if the correct output neuron does not spike despite the loss term that tries to push its spikes forward in time, there will be no valid gradient to follow. To address this issue we introduced ‘phantom spikes’ so that if the correct neuron does not spike during a trial, a regularisation loss term is added to the λ_V dynamical equation as if the neuron had spiked at time T .

4.2 Regularisation in the hidden layer

When hidden layer neurons spike too frequently or cease to spike, network performance degrades. We therefore would like to introduce a regularisation term to the loss function, as in Zenke and Vogels [55] that penalises derivations from a target firing rate,

$$\mathcal{L}_{\text{reg}} = \frac{1}{2} k_{\text{reg}} \sum_{l=1}^{N_{\text{hidden}}} \left(\left(\frac{1}{N_{\text{batch}}} \sum_{n=1}^{N_{\text{batch}}} n_l^{\text{spike},n} \right) - \nu_{\text{hidden}} \right)^2 \quad (6)$$

where $n_l^{\text{spike},n}$ denotes the number of spikes in hidden neuron l in trial n and ν_{hidden} represents the target number of spikes in a trial. For example, in the SHD experiments, $\nu_{\text{hidden}} = 14$ corresponds to a 14 Hz target firing rate in a 1000 ms trial. k_{reg} is a free parameter scaling the strength of the regularisation term. As the Eventprop formalism cannot be applied to this loss term because it cannot be expressed in a meaningful way as a function of spike times or of the membrane potential, we instead use the heuristic jumps of

$$\lambda_{V,l}^- = \lambda_{V,l}^+ - \frac{k_{\text{reg}}}{N_{\text{batch}}} \left(\left(\frac{1}{N_{\text{batch}}} \sum_{n=1}^{N_{\text{batch}}} n_l^{\text{spike},n} \right) - \nu_{\text{hidden}} \right) \quad (7)$$

at recorded spikes of hidden neuron l during the backward pass. We also trialed other regularisation terms, for instance involving per-trial spike counts but found this simple heuristic to be the most useful.

4.3 Dropout and Noise

We experimented with dropout in the input and hidden layer where input spikes occurred only with a probability $1 - p_{\text{in}}^{\text{drop}} < 1$ for each input spike and spikes in the hidden layer occurred only with probability $1 - p_{\text{hid}}^{\text{drop}}$ upon a threshold crossing. We did not observe improvements in the classification accuracy of SHD and hence did not include these mechanisms in the later parts of this work. We also experimented with additive membrane potential noise in the hidden layer, which also did not have positive effects and was subsequently omitted from the analysis.

The parameters used for the first assessments of MNIST (S1) and SHD with different loss functions (2) are detailed in tables 3, 4, 2.

4.4 Augmentations

We initially investigated four types of input augmentation to lessen the detrimental effects of overfitting.

1. The ID jitter augmentation was implemented as in Cramer et al. [6]. For each input spike, we added a $\mathcal{N}(0, \sigma_u)$ distributed random number to the index i of the active neuron, rounded to an integer and created the spike in the corresponding neuron instead.
2. In the random dilation augmentation, we rescaled the spike times of each input pattern homogeneously by a factor random factor k^{scale} drawn uniformly from $[k_{\text{min}}^{\text{scale}}, k_{\text{max}}^{\text{scale}}]$.
3. In the random shift augmentation we globally shifted the input spikes of each digit across input neurons by a distance k^{shift} uniformly drawn from $[-f_{\text{shift}}, f_{\text{shift}}]$, rounded to the nearest integer.
4. In the blend augmentation, the spikes from two randomly chosen input patterns x_1 and x_2 of the same class are “blended” into a new input pattern by including spikes from x_1 with probability p_1 and spikes from x_2 with probability p_2 . We initially trialed different combinations of $p_1 + p_2 = 1$, to restrict blending to examples from the same speaker, and blending three inputs but eventually settled on blending 2 inputs, potentially from different speakers, with $p_1 = p_2 = 0.5$. Before blending the inputs are aligned to their centre of mass along the time axis. We generated the same number of additional inputs as there were in the data set originally.

However, we observed that only the random shift augmentation and the blend augmentation improved generalisation noticeably and we conducted the remainder of the research only with these two augmentation types.

4.5 Silent neurons

In the final version of the model, we implemented a safeguard against hidden neurons becoming completely silent. Whenever a hidden neuron does not fire a single spike during an entire epoch, we add $\Delta g = 0.002$ to all of its incoming synapses. This repeats each epoch the neuron is silent but, as soon as at least one spike is fired, normal synaptic updates implementing stochastic gradient descent with Eventprop resume.

4.6 Learning rate ease-in

It is very difficult to initialise synapses so that their activity is well-suited for learning. In particular, it is often the case that the initial synaptic weights cause inappropriate levels of activity which in turn causes very large synaptic updates from the regularisation loss terms. This can lead to learning failure. The phenomenology of this problem is typically an immediate shutdown of all activity in the first few mini-batches. To avoid the problem we “ease in” the learning rate, starting with $\eta_0 = 10^{-3} \cdot \eta$ and then increasing the learning rate by a factor 1.05 each mini-batch until the full desired rate η is reached.

4.7 Learning rate schedule

In the final version of the network, we also use a learning rate schedule driven by two exponentially weighted moving averages of either the validation accuracy (in cross-validation on SHD or train/validation runs on SSC) or of the training accuracy (when running train/test on SHD),

$$m_{\text{fast}}(n+1) = 0.8 m_{\text{fast}}(n) + 0.2 x(n) \quad (8)$$

$$m_{\text{slow}}(n+1) = 0.85 m_{\text{slow}}(n) + 0.15 x(n) \quad (9)$$

where n is the epoch index and $x(n)$ is the average accuracy in the epoch. Whenever $m_{\text{fast}} < m_{\text{slow}}$, i.e. the accuracy decreased again, and at least 50 epochs have passed since the last learning rate change, the learning rate is reduced to half its value.

4.8 Heterogeneous timescale initialisation

When using heterogeneous values for τ_{mem} and τ_{syn} , we initialised the time scales from third-order gamma distributions following Perez-Nieves et al. [34],

$$\tau_{\text{mem}} \sim \Gamma(3, \bar{\tau}_{\text{mem}}/3) \tag{10}$$

$$\tau_{\text{syn}} \sim \Gamma(3, \bar{\tau}_{\text{syn}}/3) \tag{11}$$

where $\bar{\tau}_x$ are the corresponding homogeneous values used. We clipped the values to $\tau_{\text{mem}} \in [3\text{ms}, 3\bar{\tau}_{\text{mem}}]$ and $\tau_{\text{syn}} \in [1\text{ms}, 3\bar{\tau}_{\text{syn}}]$.

4.9 Learning timescales

When employing learning of timescales τ_{mem} and τ_{syn} , we use the gradient equations (37) and (39) derived in Appendix C and clip values to $\tau_{\text{mem}} \geq 3\text{ms}$ and $\tau_{\text{syn}} \geq 1\text{ms}$. There was no upper limit for the timescales during learning.

4.10 Validation methodology in ablation experiments

SHD: For each possible combination of parameters, we determined the optimal regularisation strength k_{reg} from five candidate values based on leave-one-speaker-out cross-validation with early stopping on the training error. We left all other uninvestigated parameters the same as in our reference solution and used the identified best regularisation strength for eight independent test runs with different random seeds. For these test runs, we trained on the full SHD training set and used early stopping on the epoch with the lowest training error. We then report the test accuracy for the network with the weights from this epoch.

SSC: We trained the networks for each parameter combination, five candidate regularisation strengths k_{reg} and two different random seeds on the training set and performed early stopping on the validation set. We then chose the regularisation strength for each parameter combination that led to the best average validation accuracy across the two seeds and used the corresponding weights (and τ 's if tau-learning was enabled) for inference on the test set. For each of the best regularisation choices we then ran an additional 6 repeats of training and testing to be able to report 8 independent measurements of the test error.

The parameters used for the in-depth assessment of SHD and SSC (figures 3,4) were as for the base SHD model with $\mathcal{L}_{\text{sum_exp}}$, except that we cropped the trials to $T = 1000$ ms, and used $\tau_{\text{mem}} = 20$ ms, $N_{\text{epoch}} = 100$ (no "blend") or 50 ("blend"), and the candidate values $k_{\text{reg}} \in \{5 \cdot 10^{-11}, 2.5 \cdot 10^{-10}, 5 \cdot 10^{-10}, 2.5 \cdot 10^{-9}, 5 \cdot 10^{-9}\}$ in the leave-one-speaker-out cross-validation.

4.11 Implementation details

We have used the GeNN simulator version 4.9.0 [50, 8] through the PyGeNN interface [23] for this research. Spike times and the derivative of V at the spike times are buffered in memory during the forward pass, with buffers that can hold up to 1500 spikes per two trials. The EventProp backward pass is implemented with additional neuron variables λ_V and λ_I within the neuron `sim_code` code snippet. For efficiency, we ran the forward pass of mini-batch i and the backward pass of mini-batch $i - 1$ simultaneously in the same neurons. During mini-batch 0 no backward pass is run and the backward pass of the last mini-batch in each epoch is not simulated. In initial experiments, we observed no measurable difference other than reduced runtime when compared to properly interleaved forward-only and backward-only simulations.

We obtained the SHD and SSC datasets from the tonic library [26]. During training the inputs were presented in a random order during each epoch. For the weight updates, we used the Adam optimizer [20]. The parameters of the simulations are detailed in tables 3 and 4. The simulation code is published on Github [33]. The data underlying figures 2, 3, 4, S2 and S3 are available on figshare (<https://figshare.com/s/ec4841f808ff707bed66>). Figures 1 and S1 can be recreated with minimal effort from scripts in the Github repository.

Simulations were run on a local workstation with NVIDIA GeForce RTX 3080 GPU, on the JADE 2 GPU cluster equipped with NVIDIA V100 GPUs and the JUWELS-Booster system at the Jülich

Table 2: Model parameters common to all experiments

Name	Description	Value
ϑ	firing threshold	1
V_{reset}	reset for membrane potential	0
β_1	Adam optimiser parameter	0.9
β_2	Adam optimiser parameter	0.999
ϵ	Adam parameter	10^{-8}
N_{batch}	mini-batch size	32
Δt (ms)	simulation timestep	1

Table 3: Model parameters for MNIST and loss function comparison on SHD (Fig 2)

Name	Description	Value MNIST	Value base SHD
τ_{mem} (ms)	timescale of membrane potential	20	table 4
τ_{syn} (ms)	synaptic timescale	5	table 4
T (ms)	trial duration	20	1400
μ_{i_h}	Mean initial weight value input to hidden	0.045	0.03
σ_{i_h}	Standard deviation of initial weight value input to hidden	0.045	0.01
N_{hidden}	Number of hidden neurons	128	256
μ_{h_o}	Mean initial weight value hidden to output	$\begin{cases} 0.9 & \text{if } \mathcal{L}_{\text{time}} \\ 0.2 & \text{o.w.} \end{cases}$	table 4
σ_{h_o}	Standard deviation of initial value hidden to output	$\begin{cases} 0.03 & \text{if } \mathcal{L}_{\text{time}} \\ 0.37 & \text{o.w.} \end{cases}$	table 4
μ_{h_h}	standard deviation of initial weight value hidden to hidden	–	0
σ_{h_h}	standard deviation of initial weight value hidden to hidden	–	0.02
p_{drop}	Dropout probability for input spikes	0.2	0
ν_{hidden}	target hidden spike number for regularisation	4 if $\mathcal{L}_{\text{time}}$	14
η	Learning rate	$\begin{cases} 5 \cdot 10^{-3} & \text{if } \mathcal{L}_{\text{time}} \\ 10^{-2} & \text{o.w.} \end{cases}$	table 4
τ_0 (ms)	Parameter of timing loss $\mathcal{L}_{\text{time}}$	1	1
τ_1 (ms)	Parameter of timing loss $\mathcal{L}_{\text{time}}$	3	100
α	Parameter of timing loss $\mathcal{L}_{\text{time}}$	$3.6 \cdot 10^{-4}$	$5 \cdot 10^{-5}$
N_{epoch}	number of training epochs	50	300

Supercomputer Centre, equipped with NVIDIA A100 GPUs. All runtimes are reported for A100 GPUs.

Table 4: Specific parameters of different base SHD models

Parameter	Models							
	\mathcal{L}_{sum}		$\mathcal{L}_{\text{sum_exp}}$		$\mathcal{L}_{\text{time}}$		\mathcal{L}_{max}	
loss	ffwd	recur	ffwd	recur	ffwd	recur	ffwd	recur
architecture	ffwd	recur	ffwd	recur	ffwd	recur	ffwd	recur
τ_{mem}	20	20	40	40	40	40	40	40
τ_{syn}	10	10	5	5	5	5	10	10
k_{reg}	10^{-12}	10^{-12}	10^{-10}	10^{-9}	10^{-07}	10^{-07}	$5 \cdot 10^{-9}$	$5 \cdot 10^{-9}$
μ_{h_o}	0	0	0	0	1.2	1.2	0	0
σ_{h_o}	0.03	0.03	0.03	0.03	0.6	0.6	0.03	0.03
η	0.002	0.002	0.001	0.001	0.001	0.001	0.002	0.002

Table 5: Parameters specific to augmentations (figures 3,4)

Name	Description	Value
f_{shift}	amplitude of "frequency shift" augmentation	40
N_{delay}	Number of delayed copies of input neurons	10
t_{delay} (ms)	Delay between the separate input copies	30
p_{blend}	Probability to accept a spike candidate during blending	0.5

References

- [1] Guillaume Bellec, Franz Scherr, Anand Subramoney, Elias Hajek, Darjan Salaj, Robert Legenstein, and Wolfgang Maass. A solution to the learning dilemma for recurrent networks of spiking neurons. *Nature Communications*, 11(1):3625, 2020. doi: 10.1038/s41467-020-17236-y. URL <https://doi.org/10.1038/s41467-020-17236-y>.
- [2] Alexandre Bittar and Philip N Garner. A surrogate gradient spiking baseline for speech command recognition. *Frontiers in Neuroscience*, 16:865897, 2022.
- [3] Sander M Bohte, Joost N Kok, and Han La Poutre. Error-backpropagation in temporally encoded networks of spiking neurons. *Neurocomputing*, 48(1-4):17–37, 2002.
- [4] Olaf Booiij and Hieu tat Nguyen. A gradient descent rule for spiking neurons emitting multiple spikes. *Information Processing Letters*, 95(6):552–558, 2005.
- [5] Iulia-Maria Comşa, Krzysztof Potempa, Luca Versari, Thomas Fischbacher, Andrea Gesmundo, and Jyrki Alakuijala. Temporal coding in spiking neural networks with alpha synaptic function: Learning with backpropagation. *IEEE Transactions on Neural Networks and Learning Systems*, 33(10):5939–5952, 2022. doi: 10.1109/TNNLS.2021.3071976.
- [6] Benjamin Cramer, Yannik Stradmann, Johannes Schemmel, and Friedemann Zenke. The Heidelberg Spiking Data Sets for the Systematic Evaluation of Spiking Neural Networks. *IEEE Transactions on Neural Networks and Learning Systems*, 33(7):2744–2757, 2022. doi: 10.1109/TNNLS.2020.3044364.
- [7] Manon Dampfhoffer, Thomas Mesquida, Alexandre Valentian, and Lorena Anghel. Investigating current-based and gating approaches for accurate and energy-efficient spiking recurrent neural networks. In *International Conference on Artificial Neural Networks*, pages 359–370. Springer, 2022.
- [8] GeNN developers. The GeNN repository, <https://github.com/genn-team/genn>, 2022. URL <https://github.com/genn-team/genn>.
- [9] Simone D’Agostino, Filippo Moro, Tristan Torchet, Yiğit Demirağ, Laurent Grenouillet, Niccolò Castellani, Giacomo Indiveri, Elisa Vianello, and Melika Payvand. Denram: neuromorphic dendritic architecture with rram for efficient temporal processing with delays. *Nature communications*, 15(1):3446, 2024.
- [10] Steve K Esser, Rathinakumar Appuswamy, Paul Merolla, John V Arthur, and Dharmendra S Modha. Backpropagation for energy-efficient neuromorphic computing. *Advances in neural information processing systems*, 28, 2015.
- [11] Jakub Fil and Dominique Chu. Minimal Spiking Neuron for Solving Multilabel Classification Tasks. *Neural Computation*, 32(7):1408–1429, 07 2020. ISSN 0899-7667. doi: 10.1162/neco_a_01290. URL https://doi.org/10.1162/neco_a_01290.
- [12] Răzvan V. Florian. The chronotron: A neuron that learns to fire temporally precise spike patterns. *PLOS ONE*, 7(8):1–27, 08 2012. doi: 10.1371/journal.pone.0040233. URL <https://doi.org/10.1371/journal.pone.0040233>.
- [13] J. Göltz, A. Baumbach, S. Billaudelle, A. F. Kungl, O. Breitwieser, K. Meier, J. Schemmel, L. Kriener, and M. A. Petrovici. Fast and deep neuromorphic learning with first-spike coding. In *Proceedings of the Neuro-Inspired Computational Elements Workshop, NICE ’20*, New York, NY, USA, 2020. Association for Computing Machinery. ISBN 9781450377188. doi: 10.1145/3381755.3381770. URL <https://doi.org/10.1145/3381755.3381770>.
- [14] J. Göltz, L. Kriener, A. Baumbach, S. Billaudelle, O. Breitwieser, B. Cramer, D. Dold, A. F. Kungl, W. Senn, J. Schemmel, K. Meier, and M. A. Petrovici. Fast and energy-efficient neuromorphic deep learning with first-spike times. *Nature Machine Intelligence*, 3(9):823–835, 2021. doi: 10.1038/s42256-021-00388-x. URL <https://doi.org/10.1038/s42256-021-00388-x>.
- [15] Robert Güttig. Spiking neurons can discover predictive features by aggregate-label learning. *Science*, 351(6277):aab4113, 2016. doi: 10.1126/science.aab4113. URL <https://www.science.org/doi/abs/10.1126/science.aab4113>.
- [16] Robert Güttig and Haim Sompolinsky. The tempotron: a neuron that learns spike timing–based decisions. *Nature Neuroscience*, 9(3):420–428, 2006. doi: 10.1038/nn1643. URL <https://doi.org/10.1038/nn1643>.

- [17] Ilyass Hammouamri, Ismail Khalfaoui-Hassani, and Timothée Masquelier. Learning delays in spiking neural networks using dilated convolutions with learnable spacings. *arXiv preprint arXiv:2306.17670*, 2023.
- [18] Dongsung Huh and Terrence J Sejnowski. Gradient descent for spiking neural networks. *Advances in neural information processing systems*, 31, 2018.
- [19] Jacques Kaiser, Hesham Mostafa, and Emre Neftci. Synaptic plasticity dynamics for deep continuous local learning (decolle). *Frontiers in neuroscience*, 14:424, 2020. ISSN 1662-4548. doi: 10.3389/fnins.2020.00424. URL <https://europepmc.org/articles/PMC7235446>.
- [20] Diederik P. Kingma and Jimmy Ba. Adam: A method for stochastic optimization. In Yoshua Bengio and Yann LeCun, editors, *3rd International Conference on Learning Representations, ICLR 2015, San Diego, CA, USA, May 7-9, 2015, Conference Track Proceedings*, 2015. URL <http://arxiv.org/abs/1412.6980>.
- [21] James C. Knight and Thomas Nowotny. GPUs Outperform Current HPC and Neuromorphic Solutions in Terms of Speed and Energy When Simulating a Highly-Connected Cortical Model. *Frontiers in Neuroscience*, 12, 2018. ISSN 1662-453X. doi: 10.3389/fnins.2018.00941. URL <https://www.frontiersin.org/articles/10.3389/fnins.2018.00941>.
- [22] James C Knight and Thomas Nowotny. Efficient gpu training of lsnn using eprop. In *Neuro-Inspired Computational Elements Conference, NICE 2022*, page 8–10, New York, NY, USA, 2022. Association for Computing Machinery. ISBN 9781450395595. doi: 10.1145/3517343.3517346. URL <https://doi.org/10.1145/3517343.3517346>.
- [23] James C. Knight, Anton Komissarov, and Thomas Nowotny. PyGeNN: A Python Library for GPU-Enhanced Neural Networks. *Frontiers in Neuroinformatics*, 15, 2021. ISSN 1662-5196. doi: 10.3389/fninf.2021.659005. URL <https://www.frontiersin.org/articles/10.3389/fninf.2021.659005>.
- [24] Y. LeCun and C. Cortes. Mnist database. <http://yann.lecun.com/exdb/mnist/>, 1998. URL <http://yann.lecun.com/exdb/mnist/>.
- [25] Jun Haeng Lee, Tobi Delbruck, and Michael Pfeiffer. Training deep spiking neural networks using backpropagation. *Frontiers in neuroscience*, 10:508, 2016.
- [26] Gregor Lenz, Kenneth Chaney, Sumit Bam Shrestha, Omar Oubari, Serge Picaud, and Guido Zarrella. Tonic: event-based datasets and transformations., July 2021. URL <https://doi.org/10.5281/zenodo.5079802>. Documentation available under <https://tonic.readthedocs.io>.
- [27] Sam McKennoch, Dingding Liu, and Linda G Bushnell. Fast modifications of the spikeprop algorithm. In *The 2006 IEEE International Joint Conference on Neural Network Proceedings*, pages 3970–3977. IEEE, 2006.
- [28] Ammar Mohemmed, Stefan Schliebs, Satoshi Matsuda, and Nikola Kasabov. Span: Spike pattern association neuron for learning spatio-temporal spike patterns. *International journal of neural systems*, 22(04):1250012, 2012.
- [29] Ammar Mohemmed, Stefan Schliebs, Satoshi Matsuda, and Nikola Kasabov. Training spiking neural networks to associate spatio-temporal input–output spike patterns. *Neurocomputing*, 107:3–10, 2013.
- [30] Saber Moradi, Ning Qiao, Fabio Stefanini, and Giacomo Indiveri. A scalable multicore architecture with heterogeneous memory structures for dynamic neuromorphic asynchronous processors (dynaps). *IEEE Transactions on Biomedical Circuits and Systems*, 12(1):106–122, 2018. doi: 10.1109/TBCAS.2017.2759700.
- [31] Hesham Mostafa. Supervised learning based on temporal coding in spiking neural networks. *IEEE transactions on neural networks and learning systems*, 29(7):3227–3235, 2017.
- [32] Thomas Nowotny. Two challenges of correct validation in pattern recognition. *Frontiers in Robotics and AI*, 1:5, 2014.
- [33] Thomas Nowotny. The GeNN EventProp repository, https://github.com/tnowotny/genn_eventprop, 2022. URL https://github.com/tnowotny/genn_eventprop.
- [34] Nicolas Perez-Nieves, Vincent CH Leung, Pier Luigi Dragotti, and Dan FM Goodman. Neural heterogeneity promotes robust learning. *Nature communications*, 12(1):5791, 2021.

- [35] Filip Ponulak and Andrzej Kasiński. Supervised Learning in Spiking Neural Networks with ReSuMe: Sequence Learning, Classification, and Spike Shifting. *Neural Computation*, 22(2):467–510, 02 2010. ISSN 0899-7667. doi: 10.1162/neco.2009.11-08-901. URL <https://doi.org/10.1162/neco.2009.11-08-901>.
- [36] Ran Rubin, Rémi Monasson, and Haim Sompolinsky. Theory of spike timing-based neural classifiers. *Phys. Rev. Lett.*, 105:218102, Nov 2010. doi: 10.1103/PhysRevLett.105.218102. URL <https://link.aps.org/doi/10.1103/PhysRevLett.105.218102>.
- [37] Erik Sadovsky, Maros Jakubec, and Roman Jarina. Speech command recognition based on convolutional spiking neural networks. In *2023 33rd International Conference Radioelektronika (RADIOELEKTRONIKA)*, pages 1–5. IEEE, 2023.
- [38] Mark Schöne, Neeraj Mohan Sushma, Jingyue Zhuge, Christian Mayr, Anand Subramoney, and David Kappel. Scalable event-by-event processing of neuromorphic sensory signals with deep state-space models, 2024.
- [39] Abhronil Sengupta, Yuting Ye, Robert Wang, Chiao Liu, and Kaushik Roy. Going deeper in spiking neural networks: Vgg and residual architectures. *Frontiers in neuroscience*, 13:95, 2019.
- [40] Sumit B Shrestha and Garrick Orchard. Slayer: Spike layer error reassignment in time. *Advances in neural information processing systems*, 31, 2018.
- [41] Ioana Sporea and André Grüning. Supervised learning in multilayer spiking neural networks. *Neural computation*, 25(2):473–509, 2013.
- [42] Pengfei Sun, Ehsan Eqlimi, Yansong Chua, Paul Devos, and Dick Botteldooren. Adaptive axonal delays in feedforward spiking neural networks for accurate spoken word recognition. In *ICASSP 2023 - 2023 IEEE International Conference on Acoustics, Speech and Signal Processing (ICASSP)*, pages 1–5, 2023. doi: 10.1109/ICASSP49357.2023.10094768.
- [43] Amirhossein Tavanaei and Anthony Maida. Bp-stdp: Approximating backpropagation using spike timing dependent plasticity. *Neurocomputing*, 330:39–47, 2019. ISSN 0925-2312. doi: <https://doi.org/10.1016/j.neucom.2018.11.014>. URL <https://www.sciencedirect.com/science/article/pii/S0925231218313420>.
- [44] Pete Warden. Speech commands: A dataset for limited-vocabulary speech recognition, 2018.
- [45] Yujie Wu, Lei Deng, Guoqi Li, Jun Zhu, and Luping Shi. Spatio-temporal backpropagation for training high-performance spiking neural networks. *Frontiers in neuroscience*, 12:331, 2018.
- [46] Timo C. Wunderlich and Christian Pehle. Event-based backpropagation can compute exact gradients for spiking neural networks. *Scientific Reports*, 11(1):12829, 2021. doi: 10.1038/s41598-021-91786-z. URL <https://doi.org/10.1038/s41598-021-91786-z>.
- [47] Yan Xu, Xiaoqin Zeng, Lixin Han, and Jing Yang. A supervised multi-spike learning algorithm based on gradient descent for spiking neural networks. *Neural Networks*, 43:99–113, 2013.
- [48] Yan Xu, Jing Yang, and Shuiming Zhong. An online supervised learning method based on gradient descent for spiking neurons. *Neural Networks*, 93:7–20, 2017.
- [49] Man Yao, Huanhuan Gao, Guangshe Zhao, Dingheng Wang, Yihan Lin, Zhaoxu Yang, and Guoqi Li. Temporal-wise attention spiking neural networks for event streams classification. In *Proceedings of the IEEE/CVF International Conference on Computer Vision*, pages 10221–10230, 2021.
- [50] Esin Yavuz, James Turner, and Thomas Nowotny. GeNN: a code generation framework for accelerated brain simulations. *Sci Rep*, 6:18854, 2016. doi: 10.1038/srep18854. URL <http://dx.doi.org/10.1038/srep18854>.
- [51] Bojian Yin, Federico Corradi, and Sander M Bohté. Accurate and efficient time-domain classification with adaptive spiking recurrent neural networks. *Nature Machine Intelligence*, 3(10):905–913, 2021.
- [52] Chengting Yu, Zheming Gu, Da Li, Gaoang Wang, Aili Wang, and Erping Li. Stsc-snn: Spatio-temporal synaptic connection with temporal convolution and attention for spiking neural networks. *Frontiers in Neuroscience*, 16:1079357, 2022.
- [53] Q Yu, H Tang, and H Li KC Tan. Precise-spike-driven synaptic plasticity: Learning hetero-association of spatiotemporal spike patterns. *PLOS One*, 8(11):1–16, 2013.

- [54] Friedemann Zenke and Surya Ganguli. SuperSpike: Supervised Learning in Multilayer Spiking Neural Networks. *Neural Computation*, 30(6):1514–1541, 06 2018. ISSN 0899-7667. doi: 10.1162/neco_a_01086. URL https://doi.org/10.1162/neco_a_01086.
- [55] Friedemann Zenke and Tim P. Vogels. The Remarkable Robustness of Surrogate Gradient Learning for Instilling Complex Function in Spiking Neural Networks. *Neural Computation*, 33(4):899–925, 03 2021. ISSN 0899-7667. doi: 10.1162/neco_a_01367. URL https://doi.org/10.1162/neco_a_01367.
- [56] Malu Zhang, Hong Qu, Xiurui Xie, and Jürgen Kurths. Supervised learning in spiking neural networks with noise-threshold. *Neurocomputing*, 219:333–349, 2017.

Appendix

A Full derivation of extended Eventprop

In this Appendix we present the detailed derivation for extending the EventProp algorithm to losses of the shape

$$\mathcal{L}_F = F \left(\int_0^T l_V(V(t), t) dt \right), \quad (12)$$

where F is a differentiable function and l_V can be vector-valued, e.g. $l_V = V$ as in the loss functions used in the main body of the paper.

Using the chain rule, we can calculate

$$\frac{d\mathcal{L}_F}{dw_{ji}} = \frac{\partial F}{\partial \left(\int_0^T l_V dt \right)} \cdot \frac{d \left(\int_0^T l_V dt \right)}{dw_{ji}} = \sum_n \frac{\partial F}{\partial \left(\int_0^T l_V^n dt \right)} \frac{d \left(\int_0^T l_V^n dt \right)}{dw_{ji}} \quad (13)$$

where n labels the components of the vector-valued l_V , for instance $l_V = V_{\text{output}}$ and n labels the output neurons (see below). The integrals $\int_0^T l_V^n(t) dt$ are of the shape of a classic Eventprop loss function, so we can use the Eventprop algorithm to calculate

$$\frac{d \left(\int_0^T l_V^n dt \right)}{dw_{ji}} = -\tau_{\text{syn}} \sum_{t \in t_{\text{spike}}(i)} \lambda_{I,j}^n(t), \quad (14)$$

where

$$\tau_{\text{syn}} \lambda_{I,j}^n{}' = -\lambda_{I,j}^n + \lambda_{V,j}^n \quad (15)$$

$$\tau_{\text{mem}} \lambda_{V,j}^n{}' = -\lambda_{V,j}^n - \frac{\partial l_V^n}{\partial V_j} \quad (16)$$

With this in mind, we can then calculate the gradient of the loss function (12):

$$\frac{d\mathcal{L}_F}{dw_{ji}} = -\tau_{\text{syn}} \sum_n \frac{\partial F}{\partial \left(\int_0^T l_V^n dt \right)} \sum_{t \in t_{\text{spike}}(i)} \lambda_{I,j}^n(t) \quad (17)$$

$$= -\tau_{\text{syn}} \sum_{t \in t_{\text{spike}}(i)} \sum_n \frac{\partial F}{\partial \left(\int_0^T l_V^n dt \right)} \lambda_{I,j}^n(t) = -\tau_{\text{syn}} \sum_{t \in t_{\text{spike}}(i)} \tilde{\lambda}_{I,j}(t) \quad (18)$$

where we have defined

$$\tilde{\lambda}_{I,j}(t) := \sum_n \frac{\partial F}{\partial \left(\int_0^T l_V^n dt \right)} \lambda_{I,j}^n(t). \quad (19)$$

We can then derive dynamics for $\tilde{\lambda}_{I,j}$ by simply using this definition and noting that $\frac{\partial F}{\partial \left(\int_0^T l_V^n dt \right)}$ does not depend on t ,

$$\tau_{\text{syn}} \tilde{\lambda}_{I,j}' = \sum_n \frac{\partial F}{\partial \left(\int_0^T l_V^n dt \right)} \tau_{\text{syn}} \lambda_{I,j}^n{}' = \sum_n \frac{\partial F}{\partial \left(\int_0^T l_V^n dt \right)} (-\lambda_{I,j}^n + \lambda_{V,j}^n) = -\tilde{\lambda}_{I,j} + \tilde{\lambda}_{V,j}, \quad (20)$$

where we defined

$$\tilde{\lambda}_{V,j} := \sum_n \frac{\partial F}{\partial(\int l_V^n dt)} \lambda_{V,j}^n. \quad (21)$$

That implies the dynamics

$$\tau_{\text{mem}} \tilde{\lambda}'_{V,j} = \sum_n \frac{\partial F}{\partial(\int l_V^n dt)} \tau_{\text{mem}} \lambda_{V,j}^n{}' = -\tilde{\lambda}_{V,j} - \sum_n \frac{\partial F}{\partial(\int l_V^n dt)} \frac{\partial l_V^n}{\partial V_j}. \quad (22)$$

In this fashion, we have recovered an Eventprop algorithm to calculate the gradient of the general loss function (12) by using equations (18),(20), and (22). Remarkably, this algorithm is exactly as the original Eventprop algorithm except for the slightly more complex driving term for $\tilde{\lambda}'_{V,j}$ in equation (22).

B Extended Eventprop for specific loss functions

For the concrete example of the loss function (2), we have $l_V = (V_n^m)$, i.e. the vector of output voltages of output neuron n in each batch m . With respect to the mini-batch summation we typically calculate the gradient as the sum of the individual gradients for each trial in the mini-batch,

$$\frac{d\mathcal{L}}{dw_{ji}} = \frac{1}{N_{\text{batch}}} \sum_{m=1}^{N_{\text{batch}}} \frac{d}{dw_{ji}} \left(-\log \frac{\exp\left(\int_0^T V_{l(m)}^m(t) dt\right)}{\sum_{k=1}^{N_{\text{out}}} \exp\left(\int_0^T V_k^m(t) dt\right)} \right) = \frac{1}{N_{\text{batch}}} \sum_{m=1}^{N_{\text{batch}}} \frac{dF^m}{dw_{ji}}, \quad (23)$$

with

$$F^m(\int_0^T V dt) = -\log \frac{\exp\left(\int_0^T V_{l(m)}^m(t) dt\right)}{\sum_{k=1}^{N_{\text{out}}} \exp\left(\int_0^T V_k^m(t) dt\right)} \quad (24)$$

and for each trial m and output neuron n we get

$$\frac{\partial F^m}{\partial(\int_0^T V_n^m dt)} = -\delta_{n,l(m)} + \frac{\exp(\int V_n^m dt)}{\sum_{k=1}^{N_{\text{class}}} \exp(\int_0^T V_k^m dt)} \quad (25)$$

and $\frac{\partial l_V}{\partial V_j^m} = \frac{\partial V_n^m}{\partial V_j^m} = \delta_{jn}$. We, therefore, can formulate the Eventprop scheme

$$\frac{dF^m}{dw_{ji}} = -\tau_{\text{syn}} \sum_{\{t_{\text{spike}}(i)\}} \tilde{\lambda}_{I,j}^m(t_{\text{spike}}) \quad (26)$$

$$\tau_{\text{syn}} \tilde{\lambda}_{I,j}^m{}' = -\tilde{\lambda}_{I,j}^m + \tilde{\lambda}_{V,j}^m \quad (27)$$

$$\tau_{\text{mem}} \tilde{\lambda}_{V,j}^m{}' = -\tilde{\lambda}_{V,j}^m + \delta_{j,l(m)} - \frac{\exp(\int V_j^m dt)}{\sum_{k=1}^{N_{\text{class}}} \exp(\int_0^T V_k^m dt)}. \quad (28)$$

i.e. there is a positive contribution 1 for each correct output neuron and the negative fraction of exponentials for all output neurons. All other neurons do not enter the loss function directly and the loss propagates as normal from the output neurons through the $W^T(\lambda_V^+ - \lambda_I)$ terms. The final loss is then added up according to (23).

Another typical loss function for classification works with the maxima of the voltages of the non-spiking output neurons

$$\mathcal{L}_{\text{max}} = -\frac{1}{N_{\text{batch}}} \sum_{m=1}^{N_{\text{batch}}} \log \frac{\exp\left(\max_{[0,T]} V_{l(m)}^m(t)\right)}{\sum_{k=1}^{N_{\text{out}}} \exp\left(\max_{[0,T]} V_k^m(t)\right)} \quad (29)$$

As already argued in Wunderlich and Pehle [46], we can rewrite

$$\max_{[0,T]} V_n^m(t) = \int_0^T V_n^m(t) \delta(t - t_{\text{max},n}^m) dt, \quad (30)$$

where δ is the Dirac distribution and t_{\max} the time when the maximum V was observed. Then we can use arguments as above to find the Eventprop scheme

$$\frac{dF^m}{dw_{ji}} = -\tau_{\text{syn}} \sum_{\{t_{\text{spike}}(i)\}} \tilde{\lambda}_{I,j}^m(t_{\text{spike}}) \quad (31)$$

$$\tau_{\text{syn}} \tilde{\lambda}_{I,j}^m{}' = -\tilde{\lambda}_{I,j}^m + \tilde{\lambda}_{V,j}^m \quad (32)$$

$$\tau_{\text{mem}} \tilde{\lambda}_{V,j}^m{}' = -\tilde{\lambda}_{V,j}^m + \left(\delta_{j,l(m)} - \frac{\exp(\max_{[0,T]} V_j^m)}{\sum_{k=1}^{N_{\text{class}}} \exp(\max_{[0,T]} V_k^m)} \right) \delta(t - t_{\max,j}^m), \quad (33)$$

i.e. we have jumps at the times where the maximum voltages in each of the neurons occurred, with a magnitude determined by the combination of the maximum voltages of all output neurons.

C Eventprop for neuron properties

As published, Eventprop is formulated to calculate the exact gradient with respect to synaptic weights. However, there are indications that it can be beneficial if neuron properties are heterogeneous and even trainable [34]. In this section of the Appendix we show how the Eventprop formalism can be extended to include gradient calculations for the neuron membrane time constant.

We derive the scheme by repeating the work presented in Wunderlich and Pehle [46] for the derivative $\frac{d\mathcal{L}}{d\tau_{\text{mem},i}}$. We start with the same standard Eventprop loss function, equation (1) in Wunderlich and Pehle [46] and similar dynamic equations (25), except that τ_{mem} is now individual to each neuron, i.e. $\tau_{\text{mem}} \in \mathbb{R}^n$,

$$f_V \equiv \tau_{\text{mem}} \odot \dot{V} + V - I = 0 \quad (34)$$

where \odot denotes the Hadamard product.

Then we calculate similarly to their equation (26)

$$\frac{d\mathcal{L}}{d\tau_{\text{mem},i}} = \frac{d}{d\tau_{\text{mem},i}} \left[l_p(t^{\text{post}}) + \sum_{k=0}^{N_{\text{post}}} \int_{t_k^{\text{post}}}^{t_{k+1}^{\text{post}}} [l_V(V, t) + \lambda_V \cdot f_V + \lambda_I \cdot f_I] dt \right] \quad (35)$$

but now, as we are taking the derivative with respect to $\tau_{\text{mem},i}$, equation (27a) yields

$$\frac{\partial f_V}{\partial \tau_{\text{mem},i}} = e_i \odot \dot{V} + \tau_{\text{mem}} \odot \frac{d}{dt} \frac{\partial V}{\partial \tau_{\text{mem},i}} + \frac{\partial V}{\partial \tau_{\text{mem},i}} - \frac{\partial I}{\partial \tau_{\text{mem},i}}. \quad (36)$$

This means the remainder of the proof can go ahead analogous to the original except for the extra term $\lambda_{V,i} \dot{V}_i$ within the integral between spike times (28).

It is straightforward to follow that the analogues of the jump rules up to equation (44) all carry through analogously for the derivative with respect to $\tau_{\text{mem},i}$. Then, however, when taking the derivative with respect to $\tau_{\text{mem},i}$ instead of w_{ji} in equation (46) the term $\delta_{in} \delta_{jm}$ does not arise (the partial derivative of w_{nm} with respect to $\tau_{\text{mem},i}$ is zero). So, when we put it all together and apply the equivalent smart choices for the jumps of the adjoint variables, we can eliminate all terms in the equivalent of ξ_k except for the additional $\lambda_{V,i} \dot{V}_i$, so that

$$\frac{d\mathcal{L}}{d\tau_{\text{mem},i}} = \sum_{k=0}^{N_{\text{post}}} \left[\int_{t_k^{\text{post}}}^{t_{k+1}^{\text{post}}} \lambda_{V,i} \dot{V}_i dt \right] = \int_0^T \lambda_{V,i} \dot{V}_i dt. \quad (37)$$

Similarly, if we are looking for the derivative with respect to $\tau_{\text{syn},i}$ after generalising (25b) in Wunderlich and Pehle [46] to

$$f_I \equiv \tau_{\text{syn}} \odot \dot{I} + I = 0 \quad (38)$$

with $\tau_{\text{syn}} \in \mathbb{R}^n$, we arrive at

$$\frac{d\mathcal{L}}{d\tau_{\text{syn},i}} = \int_0^T \lambda_{I,i} \dot{I}_i dt \quad (39)$$

Note that in this approach $\tau_{\text{syn},i}$ is interpreted as a property of the post-synaptic neuron, i.e. while different post-synaptic neurons can have different synaptic timescales, this is per neuron and all synaptic currents entering the same postsynaptic neuron will decay with the same timescale.

Table 6: Extended Eventprop algorithm for a wider class of loss functions and including τ learning

Loss function: $\mathcal{L}_F = l_p(t^{\text{post}}) + F\left(\int_0^T l_V(V(t), t) dt\right)$, where l_V can be a vector		
Free dynamics	Transition condition	Jumps at transition
Forward:		
$\tau_{\text{mem}} \frac{d}{dt} V = -V + I$	$(V)_n - \vartheta = 0,$	$(V^+)_n = 0$
$\tau_{\text{syn}} \frac{d}{dt} I = -I$	$(\dot{V})_n \neq 0$	$I^+ = I^- + W e_n$
Backward:		
$\tau_{\text{mem}} \lambda'_V = -\lambda_V - \frac{\partial F}{\partial (\int l_V dt)} \frac{\partial l_V}{\partial V}$	$t - t_k = 0$	$(\lambda_V^-)_{n(k)} = (\lambda_V^+)_{n(k)} + \frac{1}{\tau_{\text{mem}} (\dot{V}^-)_{n(k)}} \left[\vartheta (\lambda_V^+)_{n(k)} \right.$
$\tau_{\text{syn}} \lambda'_I = -\lambda_I + \lambda_V$		$\left. + (W^T (\lambda_V^+ - \lambda_I))_{n(k)} + \frac{\partial l_p}{\partial t_k} + l_V^- - l_V^+ \right]$
Gradient of the loss:		
$\frac{d\mathcal{L}}{dw_{ji}} = -\tau_{\text{syn}} \sum_{t \in t_{\text{spike}}(i)} \lambda_{I,j}(t)$	$\frac{d\mathcal{L}}{d\tau_{\text{mem},i}} = \int_0^T \lambda_{V,i} \dot{V}_i dt$	$\frac{d\mathcal{L}}{d\tau_{\text{syn},i}} = \int_0^T \lambda_{I,i} \dot{I}_i dt$

Supplementary material

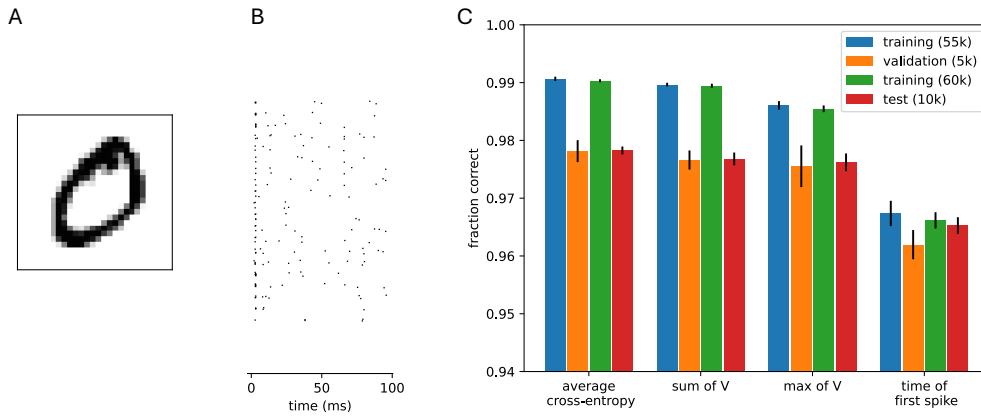


Figure S1: Overview of the classification performance of a feedforward Eventprop network on the latency encoded MNIST dataset. **A)** Example 28×28 digit from the MNIST dataset. **B)** The image from A encoded in the spike latencies t_i of neurons $i = 0, \dots, 783$, using the formula $t_i = \frac{255-x_i}{255}(T_{\text{trial}} - 4 \text{ ms}) + 2 \text{ ms}$, where x_i is the grey level of the i th pixel in a row-wise translation through the MNIST image. **C)** Classification accuracy with different loss functions. Bars are the mean of 10 independent runs and errorbars the standard deviation. All training was for 50 epochs. There was no regularisation in the hidden layer except for when $\mathcal{L}_{\text{time}}$ was used. In this case $k_{\text{reg}} = 10^{-8}$ and $\nu_{\text{hidden}} = 4$.

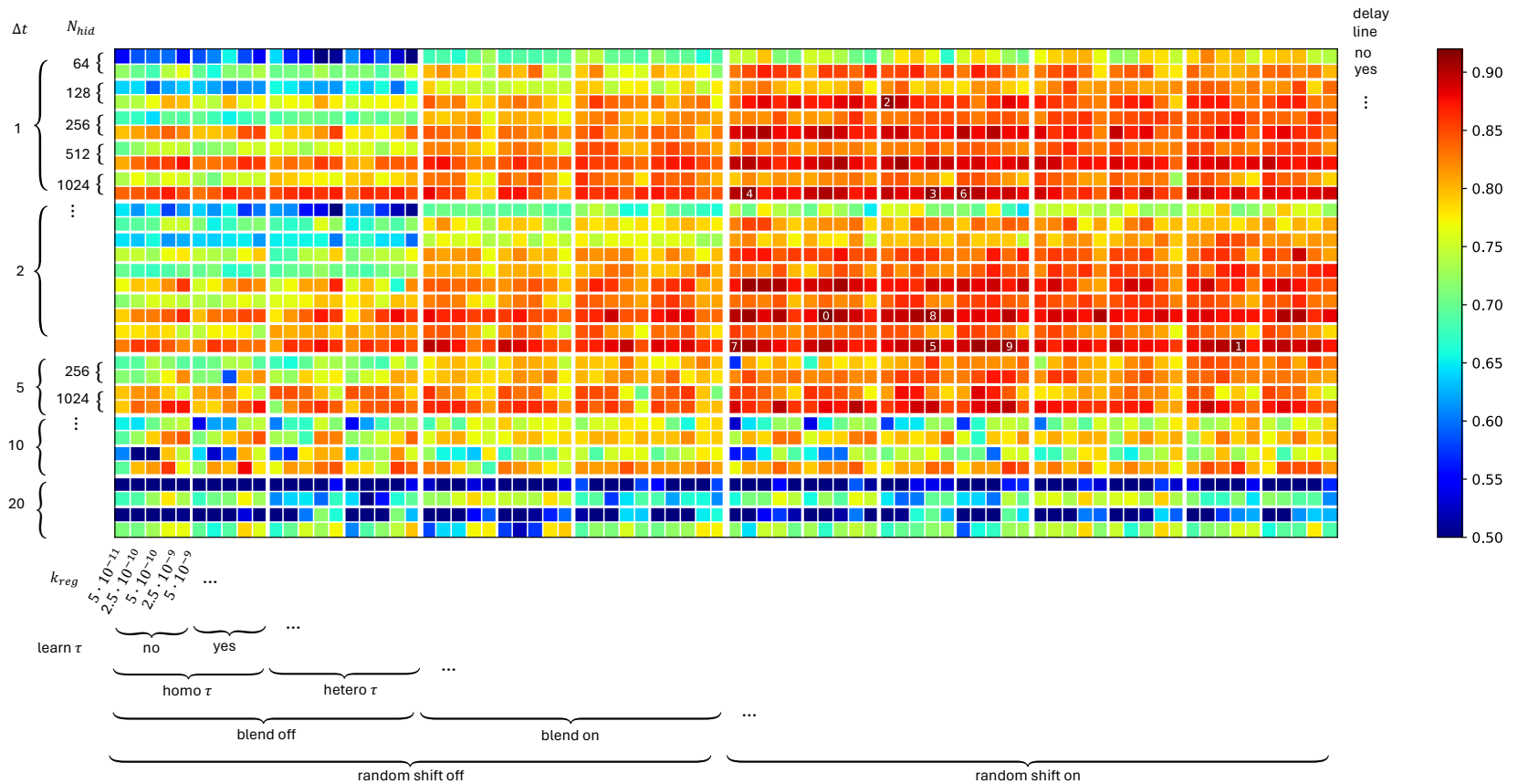


Figure S2: Overview over the final validation accuracy during 10-fold leave-one-speaker-out cross-validation on the SHD dataset. The colours code the observed validation accuracy at the epoch of best achieved training error, averaged across all 10 folds and across 2 independent runs with different seeds. The positions of the coloured cells indicate the parameter settings as indicated on the axes. The numbers 0 to 9 in white indicate the 10 best-performing parameter combinations according to this measurement. The colour range is from 0.5 to the maximal observed values to highlight differences between the well-performing networks.

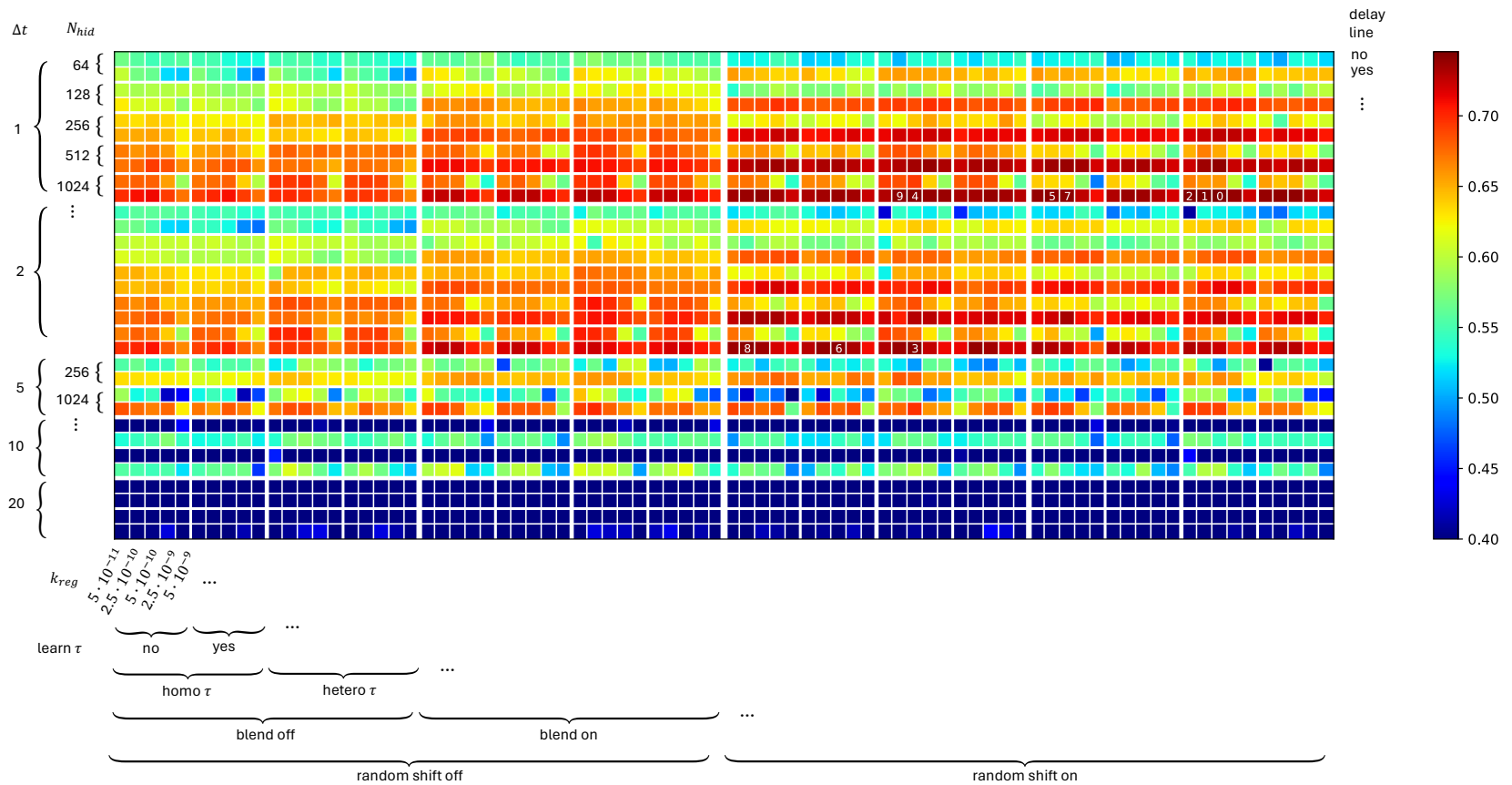


Figure S3: Overview over the best validation accuracy observed on the SSC validation set. The colours code the validation accuracy at the epoch where it is maximal, averaged across 2 independent runs with different seeds. The positions of the coloured cells indicate the parameter settings and the numbers 0 to 9 in white the best networks, as in figure S2. The colour range is from 0.4 to the maximal observed values.